A magnetic spectrometer for electron energy calibration

MacPherson, M. S.; Ross, C. K.

Publisher's version / Version de l'éditeur:
https://doi.org/10.4224/8897509
Report (Institute for National Measurement Standards (Canada). Ionizing Radiation Standards), 1998-05

A Magnetic Spectrometer for Electron Energy Calibration

M. S. MacPherson and C. K. Ross

May, 1998

PIRS-0617

Ionizing Radiation Standards
Institute for National Measurement Standards
National Research Council
Ottawa, Ontario K1A 0R6 Canada

Telephone: 613-993-9352
Fax: 613-952-9865
E-mail: carl.ross@nrc.ca

Abstract

The accurate measurement of electron stopping powers at NRC requires that the incident electron energy be known with an accuracy of better than 0.5%. Earlier work had established the energy calibration for the 90-B beam line of the National Research Council electron linear accelerator only to within 1%. As this beam line was to be employed in the stopping power measurements, a new method of calibration was required. A magnetic spectrometer has been built and adapted to the 90-B beam line. The spectrometer uses a dipole magnet to deflect the electron beam through 45°. Ray tracing calculations using detailed field maps are used to determine electron energy based on the measured magnetic field inside the magnet. The intrinsic resolution of the spectrometer is calculated to be 0.2%, while the overall estimated uncertainty in the measured energy is ±0.3%.

Measurements with the spectrometer showed that variations in the beam position and steering as it entered the 90-B analyzing magnet could lead to changes in the transmitted energy of up to 1%. The definition of the the 90-B entrance geometry was improved by adding a new set of slits, and the spectrometer was used to establish the energy calibration of the 90-B beam line. The new calibration leads to electron energies which are 0.1%, 0.9%, and 1.4% higher than predicted with the old calibration at 5, 10, and 20 MeV, respectively.

Contents

List of Figures

List of Tables

1 Introduction

The measurement of electron stopping powers at NRC uses a large, nearly totally-absorbing sodium iodide (NaI) spectrometer to measure the change in electron energy spectrum when an absorbing slab is placed in the beam. If the desired uncertainty of less than 1% in the measured stopping powers is to be achieved, then the energy calibration of the NaI spectrometer must be established to better than 1%. Unfortunately, there are no convenient radioisotopes available for calibration at the energy range of interest here (5 - 30 MeV). Consequently, the electron beam from the linear accelerator must be used to provide the energy calibration.

Earlier work has established the energy calibration of the NRC linear accelerator using electron range measurements, a photonuclear resonance in the ^{16}O γ-n reaction, and measurements of magnetic flux in the beam bending magnet. The uncertainty in the calibration resulting from these measurements was not well established, but was estimated to be about 1% (1). This level of uncertainty was deemed insufficient for this work, so a new method of energy calibration was needed.

Several calibration options were considered. Electron range measurements were not considered appropriate because of their inherent dependence on electron stopping powers (2),(3). The energy resolution associated with photonuclear resonance measurements has been shown to be about $\pm$1% (1), which is not adequate for this work. Other techniques were considered which depended on interaction kinetics to establish incident energy. These included mass scattering power measurements (4), Cerenkov threshold measurements (5), and calibrations based on measurement of the Compton distribution resulting from the interactions of bremsstrahlung photons generated by the electrons(6),(7). However, the accuracy of these methods was not expected to be greater than the range method. Magnetic spectrometry, on the other hand, has been shown to be capable of accuracies of better than 1% (8),(9). For this reason, it was decided that a magnetic spectrometer should be constructed and used to provide an energy calibration for the NRC linac. This report describes the design and operation of that spectrometer.

2 Theory

It is well known that a particle of charge q traveling with a velocity $\vec{v}$ in a magnetic field $\vec{B}$ will experience a Lorentz force $\vec{F}$ given by:

$$\vec{F} = q\vec{v} \times \vec{B}. \tag{1}$$

If the motion of the particle is perpendicular to the direction of the magnetic field, then for a constant field the motion is circular with centripetal force:

$$\frac{mv^2}{r} = qvB, \tag{2}$$

where m is the mass of the particle and r is the radius of curvature. Since $E = mc^2$ equation 2 can be written as

$$Br = \frac{Ev}{c^2 q} = \frac{E\beta}{cq},$$

where

$$\beta = \frac{v}{c} = \sqrt{\frac{E^2 - (m_o c^2)^2}{E^2}},$$

and $m_o c^2$ is the rest mass of an electron. Therefore we have,

$$Br = \frac{1}{cq}\sqrt{E^2 - (m_o c^2)^2}. \tag{3}$$

For an electron of kinetic energy T in MeV, with r expressed in cm and B in kG,

$$r = \frac{1}{0.2999B}(T^2 + 2Tm_o c^2)^{\frac{1}{2}}. \tag{4}$$

Equation 4 can be arranged to provide the kinetic energy:

$$T = \sqrt{0.08994B^2 r^2 + (m_o c^2)^2} - m_o c^2. \tag{5}$$

So the bending radius of an electron moving in a magnetic field of strength B is dependent only on its kinetic energy. For a constant magnetic field, the angle of deflection, Φ, would be given by

$$\Phi = \frac{s}{r},$$

where s is the path length through the magnet.

In a real magnet system, the field is not constant, but falls off gradually as one moves away from the pole faces. One can approximate particle transport through the magnet as if the field were constant out to a certain point, where it falls immediately to zero (figure 1). Such a point is referred to as the effective field boundary (efb) or Sharp Cut Off Fringing Field (SCOFF). Since the integral of magnetic field over the path taken is the same in each case, a particle passing through the real magnet system will undergo the same angular deflection as a particle traveling through the imaginary constant field extended to the SCOFF.

A magnet acts to focus an electron beam, in much the same way as a lens focuses light, and a full theory of magnetic optics has been developed (10),(11). The SCOFF approach forms the basis for the first-order theory of magnet optics, and provides a very good estimate of charged particle paths through a magnet system. It remains, however,t remains, however, an approximation, and if very low uncertainties are desired, as was the case with this study, then higher-order effects must be taken into account. For this work, the focusing properties of the magnet were of little consequence, as a detailed energy analysis could be performed based solely on the dispersive properties of the magnet in the horizontal plane (equation 4). Consequently, optical properties of the magnet, such as magnification and focal length, are not discussed in this report.

3 Materials and Methods

3.1 The Magnet

The magnet used for this work was a large beam-switching magnet (Anac Model 3456) which was formerly used to control the paths of ion beams emerging from the NRC Van der Graaff accelerator. The magnet comprises two low-carbon steel poles housed in a steel frame. The pole edges are tapered to reduce saturation. Surrounding the poles are two water-cooled coils wound using 5 cm (2 inch) copper tape, separated by mylar insulation between windings. The magnet is supplied with a stainless steel vacuum chamber, which provides an entrance portal and exit portals for deflections of 0°, 15°, 30°, and 45° (figure 2). In order to achieve maximum resolution, it was decided that the beam should be deflected through one of the 45°

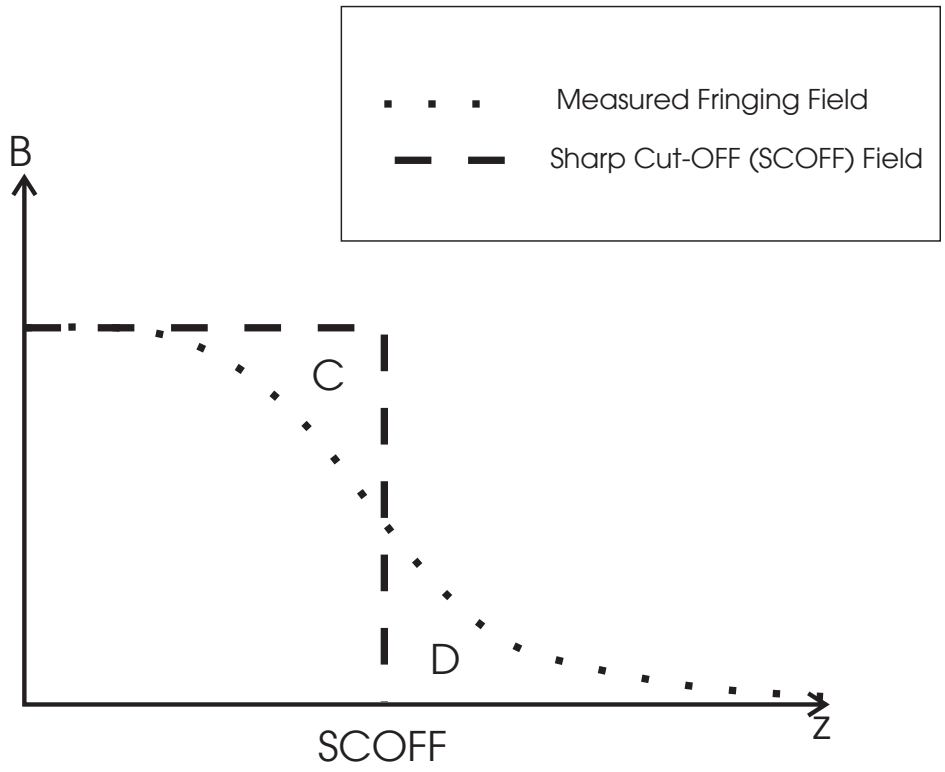

Figure 1: In the sharp cutoff approximation the areas C and D are equal, so the integral of the uniform field is the same as the integral of the real fringing field.

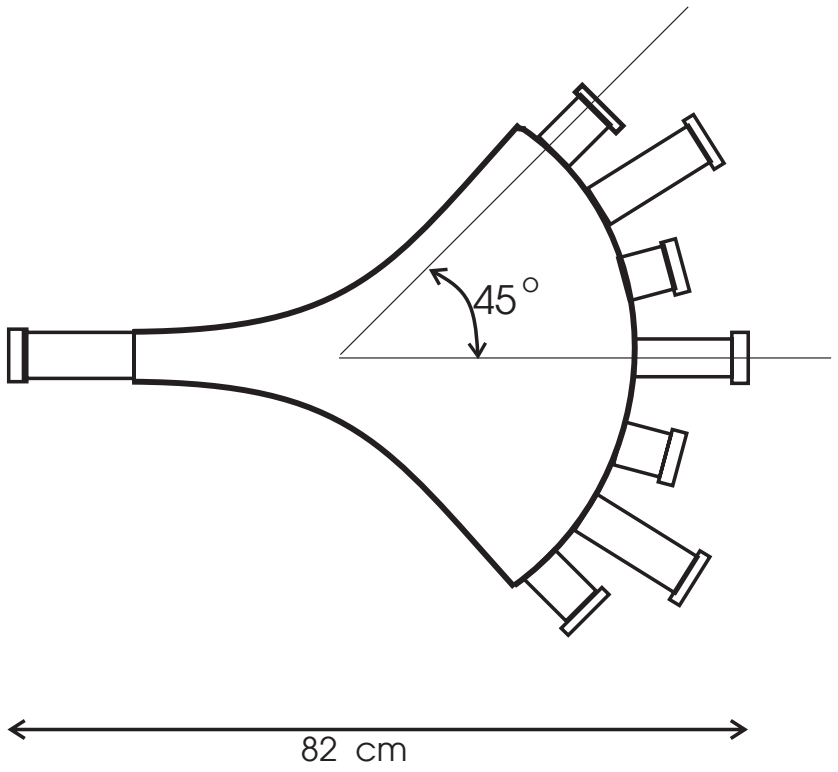

Figure 2: Schematic of the vacuum box for the Anac magnet (top view), showing beam portals for various deflections.

ports. This would provide the maximum path length in the magnet, and thus the greatest spatial separation of energies. Table 1 lists some important specifications of the magnet.

3.2 Field Mapping

One of the first objectives was to map out the relative field of the magnet over the region traversed by the electron beam. For this work, a rotating coil magnetometer was chosen over a Hall probe magnetometer, largely because of the latter's extreme sensitivity to field orientation. The magnetometer (Rawson-Lush model 924, No. 17116), consists of a 0.48 cm (3/16 inch) diameter coil rotating at the end of a long probe and sheathed in a protective aluminum cover. The coil rotates at 30 Hz producing a sinusoidal emf which is compared, via a bridge-balance, with the emf produced by a reference generator at the other end of the shaft. The relative phase between the coil and reference generator is minimized by rotating the stationary parts of the generator. The device measures only the component of the field which is perpendicular to the axis of rotation. This was advantageous in that axial components of the fringing fields, which cause no deflection, would not be measured.

The Rawson probe was mounted on an adjustable positioning stand, so that its longitudinal position could be varied by over 25 cm, with a precision of ± 0.01 cm. Lateral position could be varied by ± 2 cm, again with a precision of ± 0.01 cm.

Prior to mapping the field, it was necessary to know the effective point of measurement of the probe (i.e. the position of greatest sensitivity). The protective cover had etchings which were supposed to indicate the centre of the coil, but it was not known how well the etchings correlated with the actual coil position. Furthermore, the large size of the coil called into question its spatial resolution.

Conical pole faces were machined for a permanent magnet, as shown in figure 3. The magnetic flux between these pole faces was expected to be very high between the vertices of the cones, and then fall off rapidly. The probe was moved between the pole faces, and the magnetic field as a function of position was recorded. A 3 mm offset was noticed between the etchings on the probe and the apparent centre of the magnet. The procedure was repeated with a Rawson probe with a much smaller coil ($\frac{1}{8}$ inch diameter), and no offset was observed, indicating that the coil of the large probe was in fact offset from the etchings by 3 mm. Closer

Field	0 - 1.65 Tesla [a]
Pole Gap	3.025 cm [b]
Angular Deflection	44.943° [b]
Exit Shim Angle	26.28° [a]
Entrance Shim Angle	0° [a]
Bending Radius (45°)	45.36 cm [b]

Table 1: Specifications of spectrometer magnet. [a] denotes manufacturer's specifications; [b] indicates the quantity is based on in-house measurements.

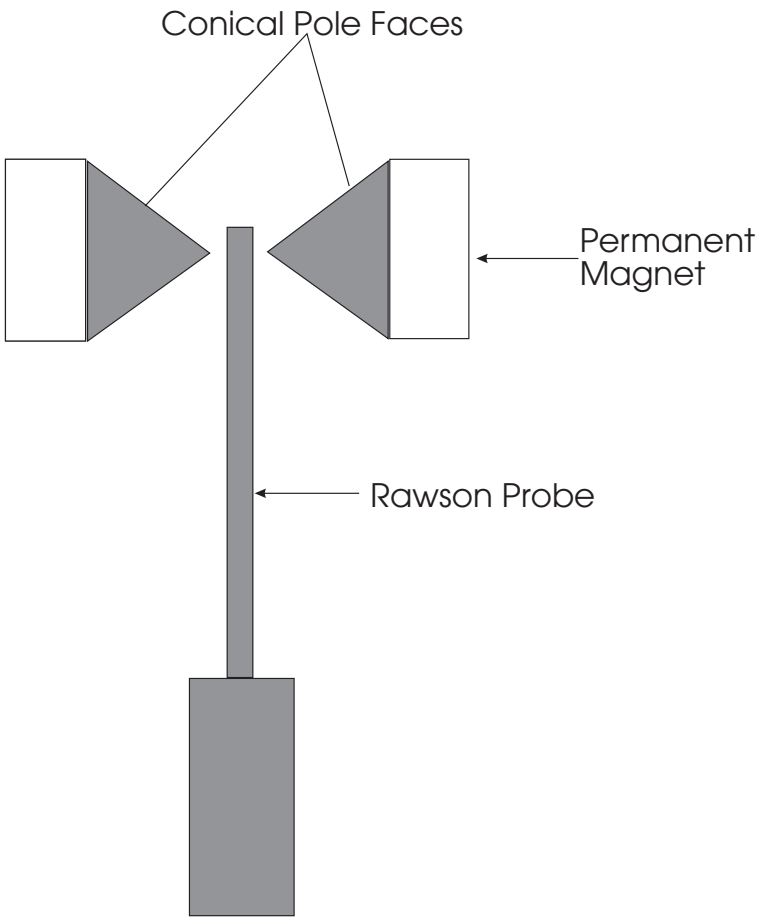

Figure 3: Schematic of permanent magnet arrangement used to determine the effective point of measurement for the Rawson probes (top view).

examination of the rotating shaft indicated that this was indeed the case, and the problem was corrected. Figure 4 shows the results of these measurements after correcting the offset in the large coil. The close agreement between the small coil probe and the large coil probe indicated that the larger coil width did not significantly broaden the shape of the flux density curve, so spatial resolution was not considered a significant problem.

The magnet was provided with an aluminum alignment plate, which could be attached to the bottom pole face (field mapping was performed without the vacuum box in place). Grooves were machined in the plate which corresponded to the rays of the final paths the particles would travel if deflected by the field. In order to facilitate alignment, an aluminum tube was fitted with cross hairs at each end. The tube sat in the alignment grooves, providing a means of visually aligning with the magnet. With the alignment tool in place, the Rawson probe was sighted along the paths the electrons were expected to take, i.e. with the normal entrance position, and along the 45° exit position. In order to determine the position of the probe, a pin was placed at the vertex of the alignment plate (the intersection of the 0° and 45° grooves), and an aluminum rod of known length was placed in the alignment groove so as to be just touching the end of the probe and the vertex pin. In this way, measurement position was determined to better than ±0.5 mm.

Field measurements were performed in the fringing field regions as well as inside the pole faces, where the field was expected to be constant. Readings were taken at intervals of 2.5 mm. In addition to measurements along the central axes, measurements were taken at horizontal and vertical offsets of ±1 cm to ensure that the relative fields did not change unexpectedly in any region the electron beam could conceivably cross. Field mapping was performed at two different field settings (≈ 0.2 and 0.4 T) to ensure that the shape of the relative field was independent of field strength for the magnetic fields considered here. The relative fields were equal within 0.1 mm (figure 5), yielding identical sharp cut-offs. Since the fields of interest in this study are significantly lower (0.07 to 0.3 T), one can assume that saturation effects are not important in the fringing field region.

The measured fringing fields are shown in figure 6. No difference greater than 0.1% was found between fields measured along the central axis, and those measured at displacements of ±1 cm on the horizontal and vertical axes. Integrating the entrance fringing fields yielded a

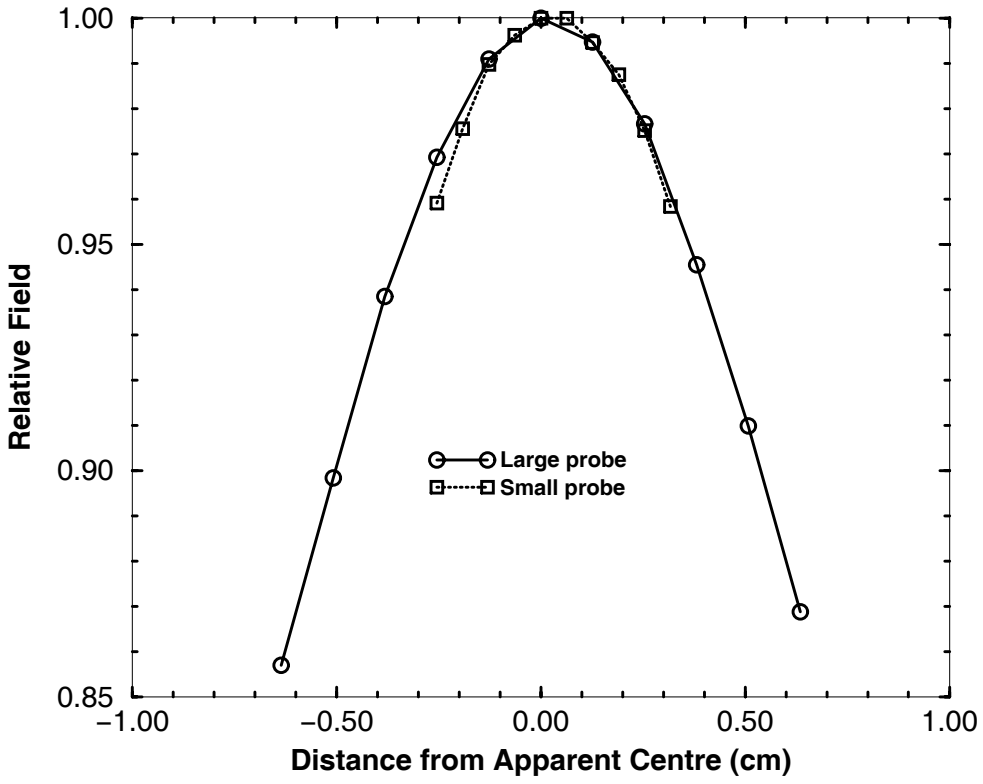

Figure 4: The effective point of measurement for each Rawson magnetometer was determined by passing it between a permanent magnet with conical pole faces. No significant broadening was introduced by the larger probe.

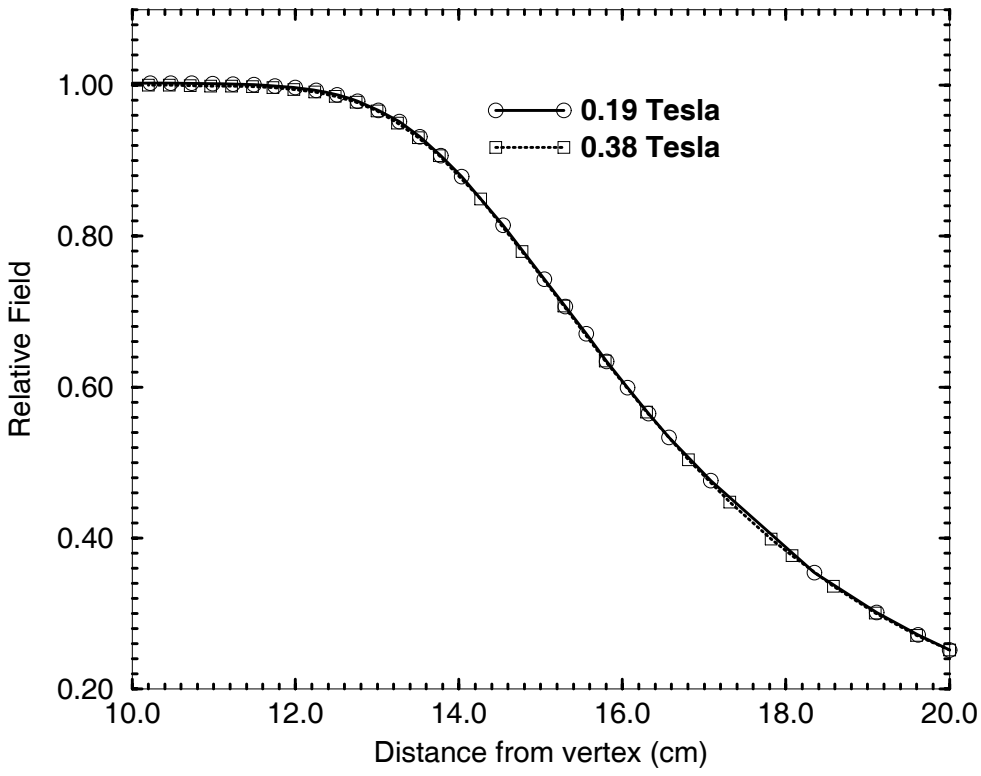

Figure 5: Measured exit fringing fields at two different field values. The relative fields are in excellent agreement, demonstrating that saturation effects are not important at the field levels considered in this study.

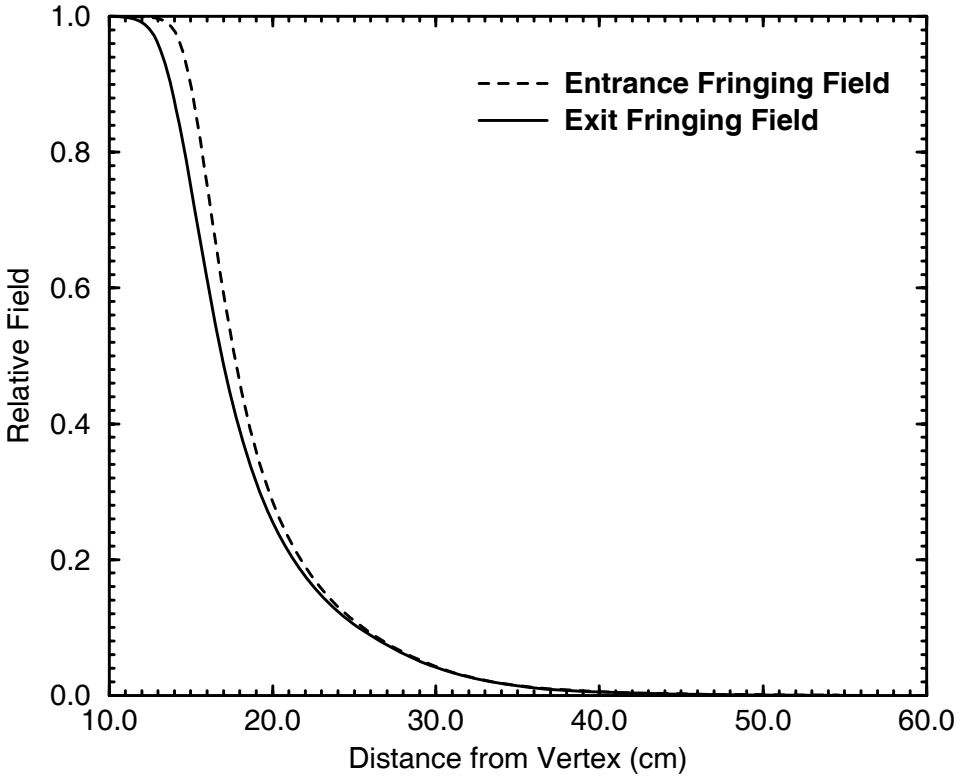

Figure 6: Comparison of entrance and exit fringing fields.

SCOFF of 19.11 ± 0.05 cm from the vertex of the alignment plate, in rather poor agreement with the manufacturer's value of 18.88 cm. Similarly, the exit SCOFF was measured to be 18.44 ± 0.05 cm from the vertex, rather than 18.63 cm as suggested by the manufacturer. Detailed mechanical measurements revealed that the position of the vertex of the alignment plate did not correspond to the position quoted by the manufacturer in the manual. The size of the offset (approximately 1 mm in the backward direction) is consistent with the discrepancies noted in the fringing field measurements. However, if the sharp cut-off is quoted with respect to the edge of the pole faces, the measured results of 4.8 ± 0.05 mm on the entrance side and 5.5 ± 0.05 mm on the exit side agree reasonably well with the manufacturer's values of 5.9 mm and 5.6 mm, respectively. Moreover, if the measured field is integrated to determine the actual bending radius, the measured result of 45.36 cm is in good agreement with the design value of 45.29 cm, leading to a difference in transmitted energy of only 0.15%.

Inside the pole faces, where the field was expected to be constant, the field was noticed to increase steadily as the probe was moved from the entrance to the exit side of the pole faces (figure 7). This is probably due to the sector shape of the magnet, which results in more magnetic material at the exit side. While the magnitude of the change was small, it was considered significant enough to be included in later analysis.

The stainless steel vacuum box was not expected to perturb greatly the magnetic field inside the pole faces. To test this, several mock-ups of the vacuum assembly were made using stainless steel tubes and boxes of the approximate thickness of the vacuum box. Magnetic field measurements with and without the stainless steel were consistent within ±0.05%. The perturbation caused by the vacuum box also can be estimated based on the relative permeability of stainless steel.

The magnet poles, vacuum box, and air gap comprise a magnetic circuit (figure 8). The magnetic flux of the circuit is equal to the magnetomotance NI divided by the reluctance $\mathcal{R}$. With the vacuum box in place, the flux is (12):

$$\Phi_1 = \frac{NI}{\frac{L_p}{\mu_p A} + \frac{L_{box}}{\mu_{box} A} + \frac{L_{air}}{\mu_{air} A}}, \tag{6}$$

where the subscript p refers to the poles, A is the area through which the flux density will

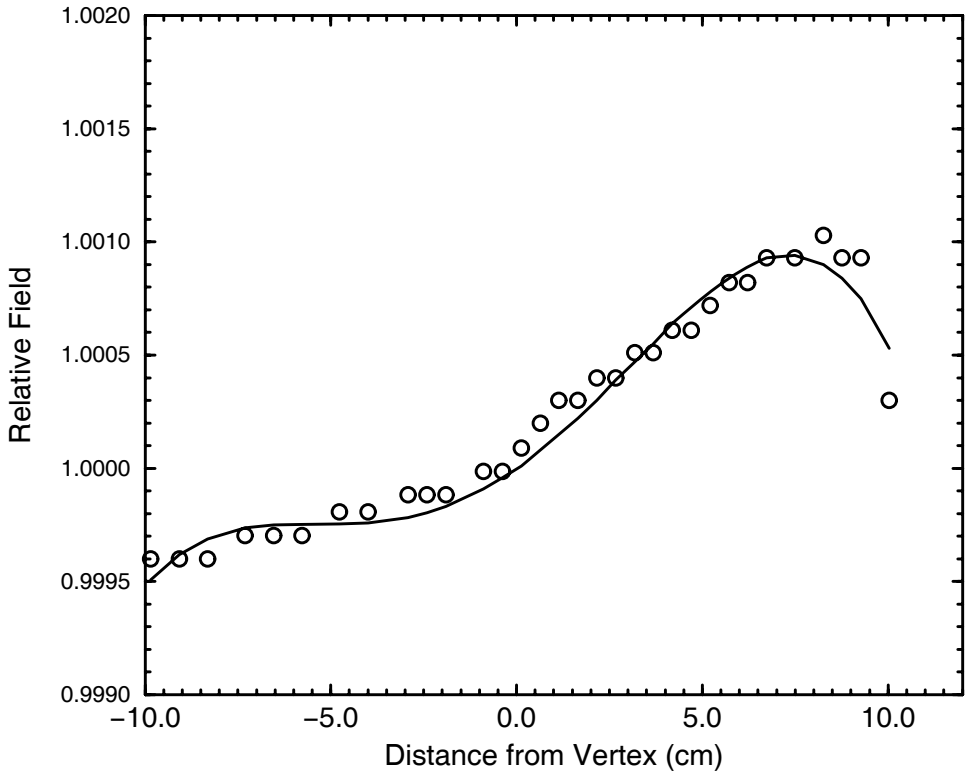

Figure 7: Field inside pole faces increases toward exit side. The measured field has been fit with a polynomial for use in analysis.

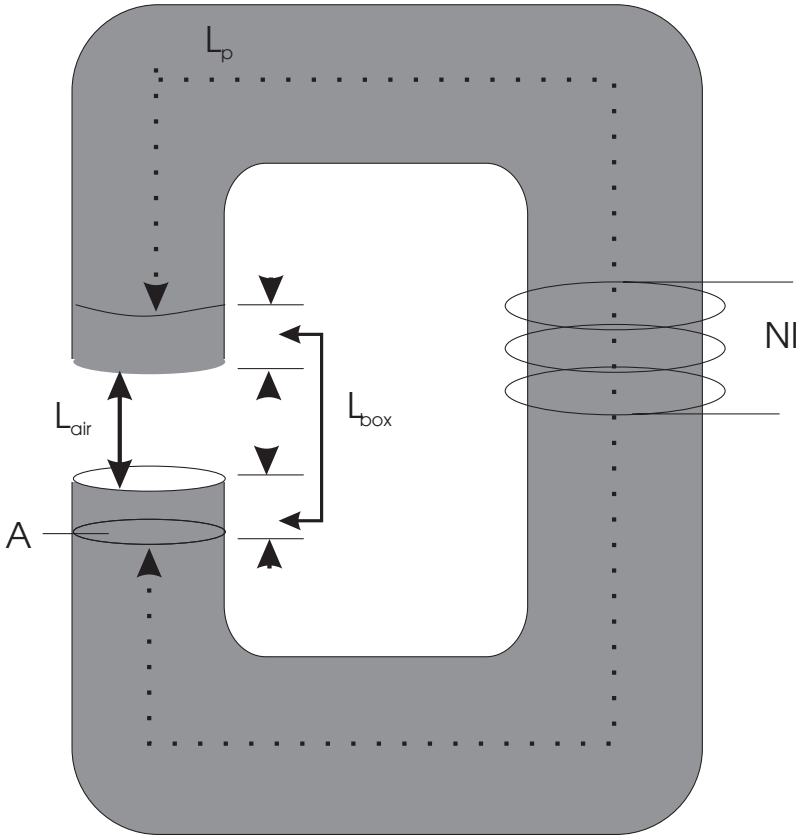

Figure 8: Schematic of spectrometer as a magnetic circuit.

be measured (i.e. the pole faces). L_p can be measured around the supporting frame.

If the box is removed, then the flux becomes:

$$\Phi_2 = \frac{NI}{\frac{L_p}{\mu_p A} + \frac{L_{box}}{\mu_{air} A} + \frac{L_{air}}{\mu_{air} A}}. \tag{7}$$

So the ratio of fluxes is:

$$\frac{\Phi_1}{\Phi_2} = \frac{\frac{L_p}{\mu_p} + \frac{L_{box}}{\mu_{box}} + \frac{L_{air}}{\mu_{air}}}{\frac{L_p}{\mu_p} + \frac{L_{box}}{\mu_{air}} + \frac{L_{air}}{\mu_{air}}}. \tag{8}$$

Considering that $\mu_{box} \approx 1.00005$ and that $\mu_p \approx 10^5$, we find that $\frac{\Phi_1}{\Phi_2} = 1.00003$. Therefore it is safe to assume that the presence of the vacuum box does not perturb the measured field.

3.3 Ray Tracing

If the magnetic field produced by the magnet were constant inside the pole faces and zero everywhere else, then the problem of extracting electron energy would be trivial (equation 5). This is essentially the SCOFF approach. However, since the field falls off gradually in the fringing field regions, the bending radius changes continuously there, and the true path of an electron of kinetic energy T is no longer circular. This problem can be overcome by realizing that over a small element of path length the field is constant, and the path can be considered circular within that element. Summing over several such elements constitutes, in effect, integration of the equations of motion. Such a technique is known as *ray tracing*. Two approaches to the ray tracing problem were taken for this work. Initially, a FORTRAN program, called ESPLINE, was written to simulate the passage of electrons through the magnet based on measured fringing field data. For more detailed analysis, the program RAYTRACE was used (13).

3.3.1 Program ESPLINE

The algorithm for ESPLINE is as follows. Fringing field data are read in as coordinate pairs of distance from the magnet vertex (i.e. intersection of entrance and exit rays) and magnetic field relative to the magnetic field at the magnet vertex.

The electron is initialized in terms of its energy T, position (x, y), and direction cosine with respect to the central axis (figure 9). The user is then prompted to enter a step size, δ, and magnetic field in kG. The electron then moves a distance δ in its original direction. That is:

$$x' = x + \delta \cos\Phi,$$

$$y' = y + \delta \sin\Phi.$$

If the particle is in the fringing field regions, the magnetic field at the centre of the step is determined by cubic spline interpolation of the measured fringing field data, otherwise, the maximum field is assumed. The bending radius is then determined by equation 4. Since the bending radius r is orthogonal to the motion everywhere, the new angle will be

$$\Phi = \Phi + \Delta\Phi,$$

where

$$\Delta\Phi = \tan^{-1}\left(\frac{\delta}{r}\right).$$

The position (x, y) and angle Φ are written out at each step. The process continues until the electron leaves the fringing field region and the program terminates. ESPLINE was useful in determining the basic behaviour of electrons passing through the magnet. For instance, it was able to determine the approximate slit size necessary to achieve adequate resolution (2 mm for 0.2%). However, the algorithm was too simplistic to provide the level of accuracy desired for this work. For example, the shape of the pole faces was not taken into account; the magnet was essentially treated as being circular with 0^o shim angles everywhere. Moreover, no provision was made for the simulation of radial magnetic field components. A more physically rigorous approach to the ray tracing problem was needed.

3.3.2 Program RAYTRACE

RAYTRACE (13) was developed at the Massachusetts Institute of Technology (MIT) for the design of beam transport systems. It is a general use code which allows the simulation of ions through various ion-optical components, including dipole magnets. Complex pole shapes and magnetic fields can be entered parameterically. RAYTRACE simulates ion transport

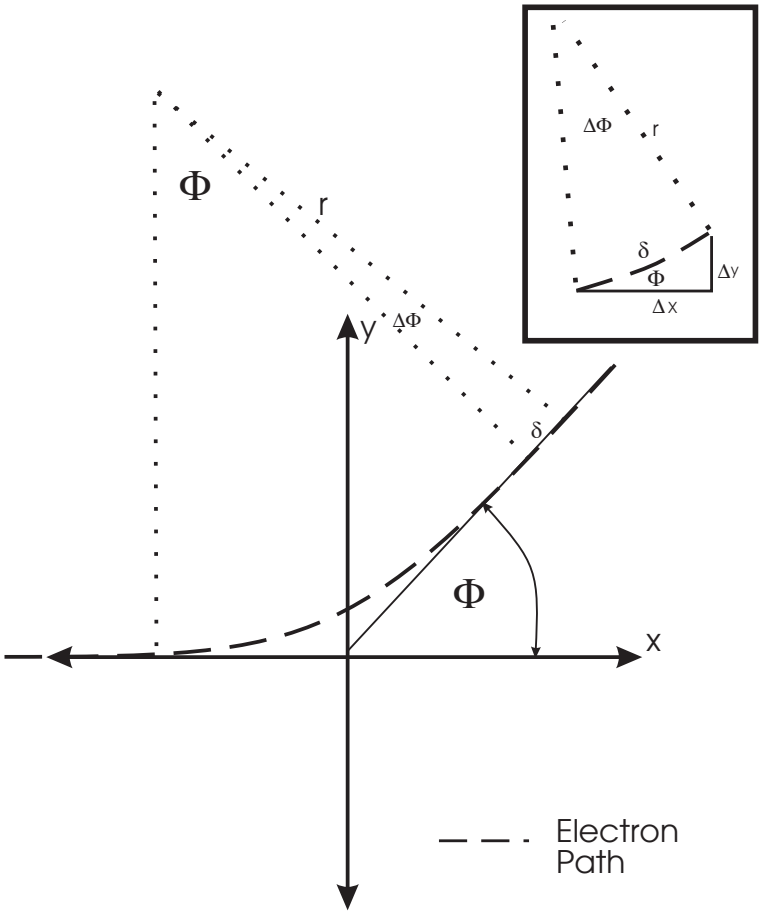

Figure 9: Geometry for ESPLINE ray tracing program. If δ is small enough the path is nearly straight.

by performing a fourth order Runge-Kutta integration of the equations of motion resulting from equation 1.

Median plane transverse magnetic field data are entered as input, and components of the magnetic field off the median plane are calculated for all three directions and included in the simulation. In order to calculate components of magnetic field off the median plane, RAYTRACE takes advantage of the symmetry of the dipole magnet (figure 10). The magnetic field components can each be expressed as a Taylor series expansion in the transverse direction, y (figure 10). By symmetry, we know that the transverse (y) component will have only even terms, while the longitudinal (x and z) components will have only odd terms. To third order, then, the expressions are given by (13):

$$B_x(y) = y\frac{\partial B_x}{\partial y} + \left(\frac{y^3}{3!}\right)\frac{\partial^3 B_x}{\partial y^3}, \tag{9}$$

$$B_y(y) = B_y + \left(\frac{y^2}{2!}\right)\frac{\partial^2 B_y}{\partial y^2} + \left(\frac{y^4}{4!}\right)\frac{\partial^4 B_y}{\partial y^4}, \tag{10}$$

and

$$B_z(y) = y\frac{\partial B_z}{\partial y} + \left(\frac{y^3}{3!}\right)\frac{\partial^3 B_z}{\partial y^3}, \tag{11}$$

where the terms are evaluated on the median plane (y=0). From Maxwell's equations, we know that

$$\nabla \cdot \vec{B} = 0, \tag{12}$$

and also that

$$\nabla \times \vec{B} = 0 \tag{13}$$

for a steady state field with no residual magnetization or electric field. We can rewrite equation 12 as

$$\frac{\partial B_y}{\partial y} = -\left(\frac{\partial B_x}{\partial y} + \frac{\partial B_z}{\partial y}\right). \tag{14}$$

From equation 13 we know that

$$\frac{\partial B_x}{\partial y} = \frac{\partial B_y}{\partial x},$$

and

$$\frac{\partial B_z}{\partial y} = \frac{\partial B_y}{\partial z}.$$

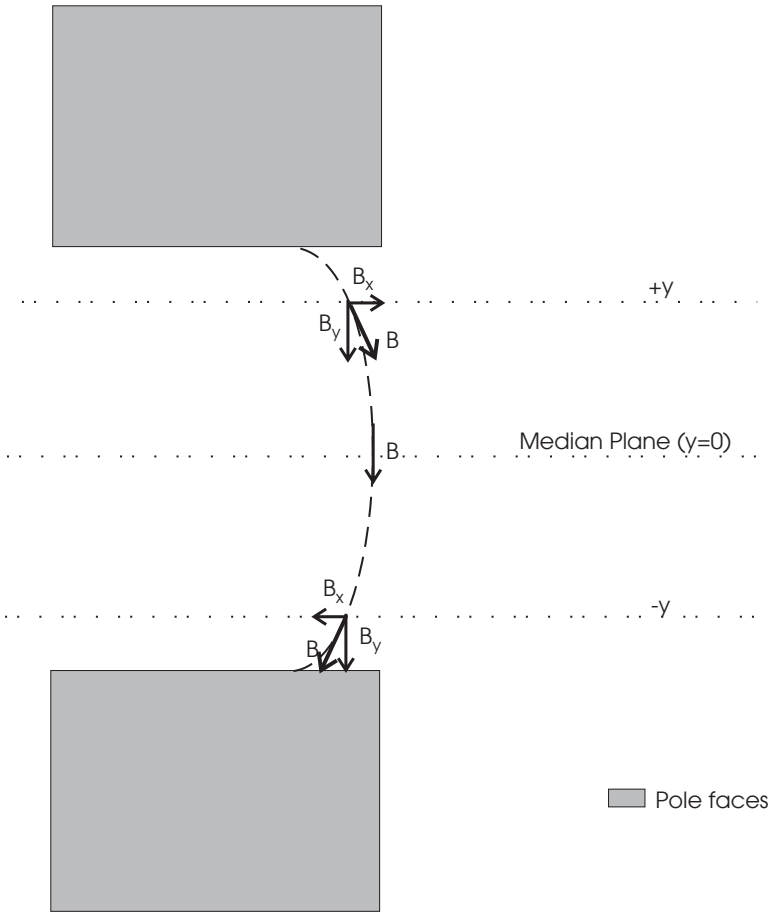

Figure 10: Sample magnetic field line between pole faces. By symmetry, the y component of the magnetic field is an even function of y about the median plane. The x and z components are odd functions.

This means that partial derivatives of B_x and B_z can be calculated only from changes of the transverse field, B_y in the median (x-z) plane. This is fortunate, since the only input data are parameterizations of B_y as a function of z in the entrance and exit coordinate systems. Parallel paths in the entrance and exit coordinate system are assumed to have the same parameterization of field (this is consistent with the measurements reported in section 3.2). Changes in B_y in the median plane are calculated using a 13 point grid (figure 11) which is aligned along the direction of the electron. Grid point separations of 1 cm inside the poles and 0.3 cm in the fringing field region are used. Derivatives in x and z are determined numerically from this grid, and used to evaluate equations 9, 10 and 11. When the electron is moving parallel to the entrance or exit z axis, many of the the partial derivatives are zero. This is also true when the electron is in the uniform field region. However, when an electron is in the fringing field region these derivatives are non zero. The deflections calculated using these off-axis fields are very small (typically less than 2 mm for reasonable entrance offsets).

The geometry of RAYTRACE is quite complex, and merits some discussion here. For a more detailed discussion of the geometry, the reader is referred to the RAYTRACE manual (13). The magnetic element is considered to consist of three distinct regions: an entrance fringing field region (AB), a uniform field region (BC), and an exit fringing field region (CD)(figure 12). Each region has its own coordinate system, in addition to the entrance and exit coordinate systems. All calculations are made with respect to a region's coordinate system. Transformations to new systems are performed at predefined crossover points. The sharp cut-offs of the magnet are used to establish the BC coordinate system. The design radius, r, is taken as the bending radius for a particle moving through the SCOFF field of strength B_o. The shim angles α and β represent the angle made between the ion beam and the SCOFF field, which follows the shape of the pole faces. The curvature of the pole faces can either be parameterized by a polynomial, or by the radius of curvature for a sector magnet such as the one used in this study.

Measured fringing fields are entered as six coefficients, C00 ... C05 for the entrance fields and C10 ... C15 for the exit fields. The coefficients are obtained by least-squares fitting the measured field data to

$$B_y = \frac{B_o - B_R}{1 + e^S} + B_R, \tag{15}$$

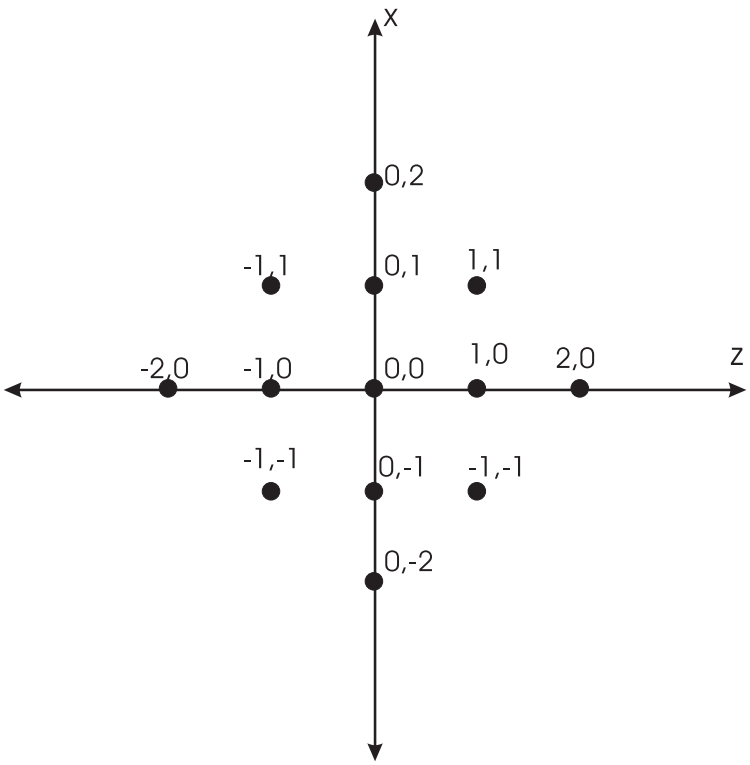

Figure 11: The thirteen point grid used to determine off-axis field components. The coordinates refer to array indices; the true spacing is determined by the user. The grid is aligned with the electron's direction of motion (z-axis).

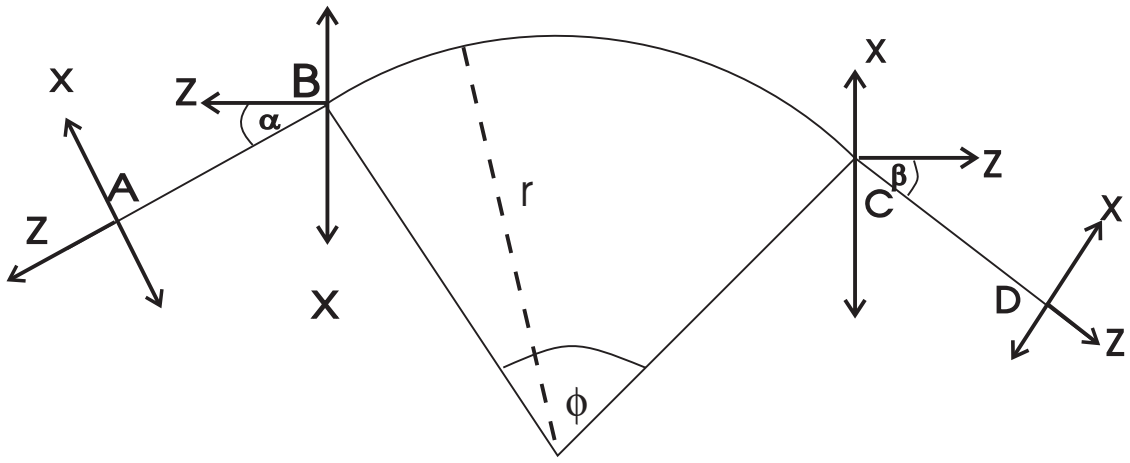

Figure 12: Geometry for RAYTRACE . The effect of the field is evaluated in the entrance fringing field (AB), the uniform field (BC), and the exit fringing field (CD).

where B_o is the uniform field, B_R is a constant background field, and

$$S = C00 + C01s + C02s^2 + C03s^3 + C04s^4 + C05s^5.$$

Here

$$s = \frac{z}{D},$$

where z is the distance from the SCOFF and D is the pole gap. The user must also specify the extent of the fringing field in each direction (both into and out of the magnet) beyond the sharp cutoff points B and C. The extremes of the fringing fields define the crossover points, where RAYTRACE performs coordinate system transformations. The field nonuniformity depicted in figure 7 was parameterized by a 3$^{\text{rd}}$ order polynomial from which field values inside the pole faces were calculated. In this case, B_o refers to the field at the vertex.

RAYTRACE reports the final position in terms of the coordinate system D, which is defined by the ray resulting from deflection of a particle with energy T given by equation 5 through the SCOFF field. This makes interpretation of the results slightly more complicated because, as has already been stated, the SCOFF rays do not correspond to the alignment plate.

Figure 13 depicts the effect of using the SCOFF field to determine the final path of the electron. The SCOFF rays are shown as bold lines. The dashed lines represent the rays projected by the alignment plate. This essentially results in two frames of reference: a SCOFF frame and an alignment plate frame. For each coordinate system, the angle of deflection is the same. However, the exit path of the electron in the alignment plate frame is offset from the SCOFF path by an amount $\Delta x'$. The problem is exacerbated if the electron does not exit the magnet at right angles, but rather at some shim angle β.

If the distance from the vertex to the exit effective field boundary in the alignment frame of reference is R_{out}, then the distance R'_{out} from the SCOFF vertex to the effective field boundary is

$$R'_{out} = R_{out} + \Delta x \cos\Phi + \Delta x \sin\Phi \tan\beta.$$

For the entrance ray we have

$$R'_{in} = R_{in} - \Delta x.$$

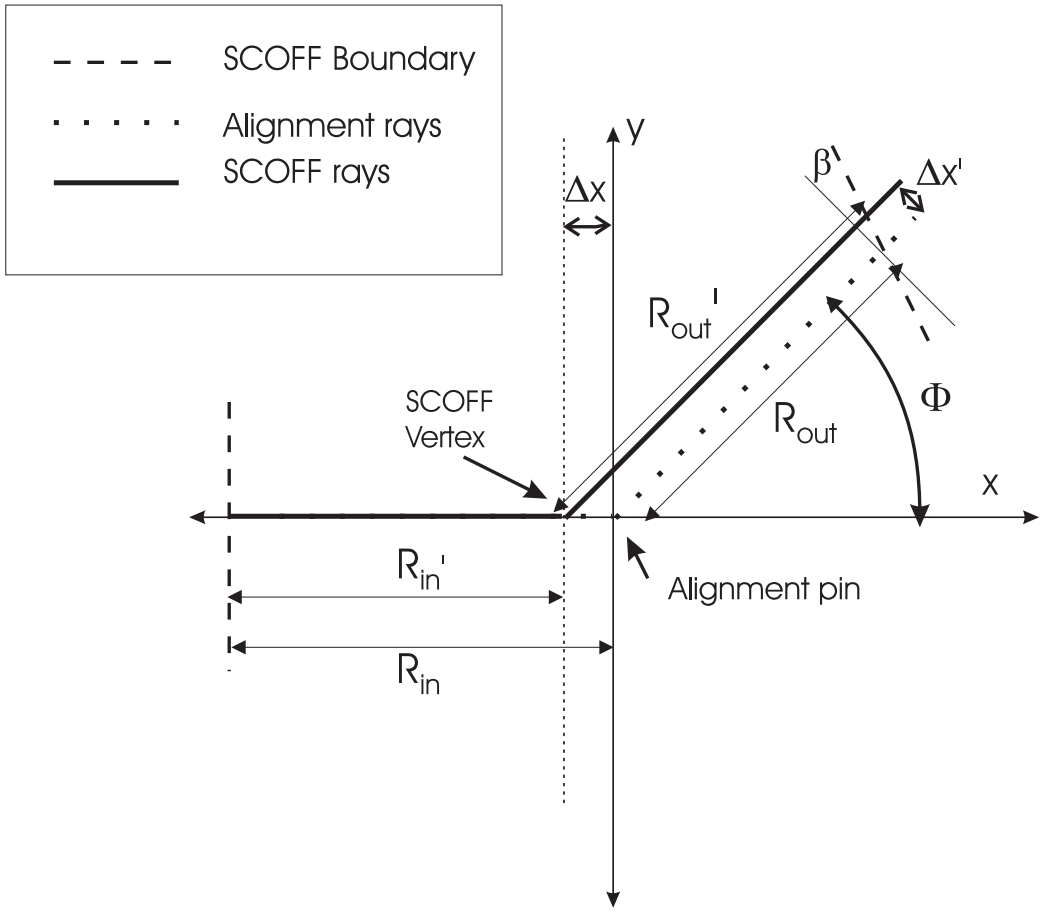

Figure 13: Measurements made in the alignment frame of reference (dotted lines) are used to determine the SCOFF of reference required for RAYTRACE calculations (solid lines). The two coordinate systems are offset by an amount Δx.

By symmetry, we expect $R'_{out} = R'_{in}$ (*i.e.* the SCOFF rays are equal) so substituting $\Phi = 45^o$, $\beta = 26.28^o$, and measured values for R_{in} and R_{out} gives $\Delta x = 0.33$ cm so $\Delta x' = 0.22$ cm. The SCOFF rays are each 18.79 cm (from vertex to SCOFF boundary). This also yields the first-order bending radius, r, (used in equation 5) which is 45.36 cm.

This means that an electron with bending radius r in the SCOFF field will actually emerge 2.2 mm to the right of the ray established by the alignment plate. Put another way, the paths of interest from RAYTRACE simulations are those which exit the magnet system with an x offset of 2.2 mm from the D coordinate system. For the energies considered here, a 2.2 mm offset can represent a 0.2% change in energy.

In the final analysis, RAYTRACE simulations were used to convert measured magnetic field spectra to electron energy spectra. Table 2 compares the magnetic field required to deflect an electron through the rays defined by the alignment plate (as calculated by RAYTRACE) with the field required to deflect an electron through 45° in the SCOFF approximation. Note that the fields are equal within 0.1%. While the RAYTRACE electron exits the magnet at the correct *position*, its direction differs from the SCOFF electron by several milliradians. This has no impact on the energy analysis, however, since transmission of the electron is all that is required for spectrometry. A corollary of this result is that the user may employ first order analysis (equation 5) without compromising accuracy. The reason for this can be seen by comparing the actual path of an electron through the true field with the circular path it would take in the SCOFF approach, as shown schematically in figure 14. In the real field, the electron is deflected long before the SCOFF by the entrance fringing fields. The radius of curvature changes constantly outside the uniform field region, leading to offsets inside the magnet. Outside the magnet, the exit fringing field continues to deflect the electron with a constantly changing radius of curvature, so that the true ray crosses the SCOFF ray about 6 mm past the effective field boundary with a relative angle of -2°. By the time the electron leaves the fringing field, it is offset from the SCOFF ray by approximately 2 mm with a relative angle of 0.1°.

Electron Energy (MeV)	RAYTRACE Field (kG)	SCOFF Field (kG)
5.00	0.405	0.405
10.03	0.775	0.774
20.05	1.512	1.512
30.01	2.245	2.244
40.00	2.980	2.979

Table 2: Comparison of calculated field required to give transmission with SCOFF field needed to give 45° deflection.

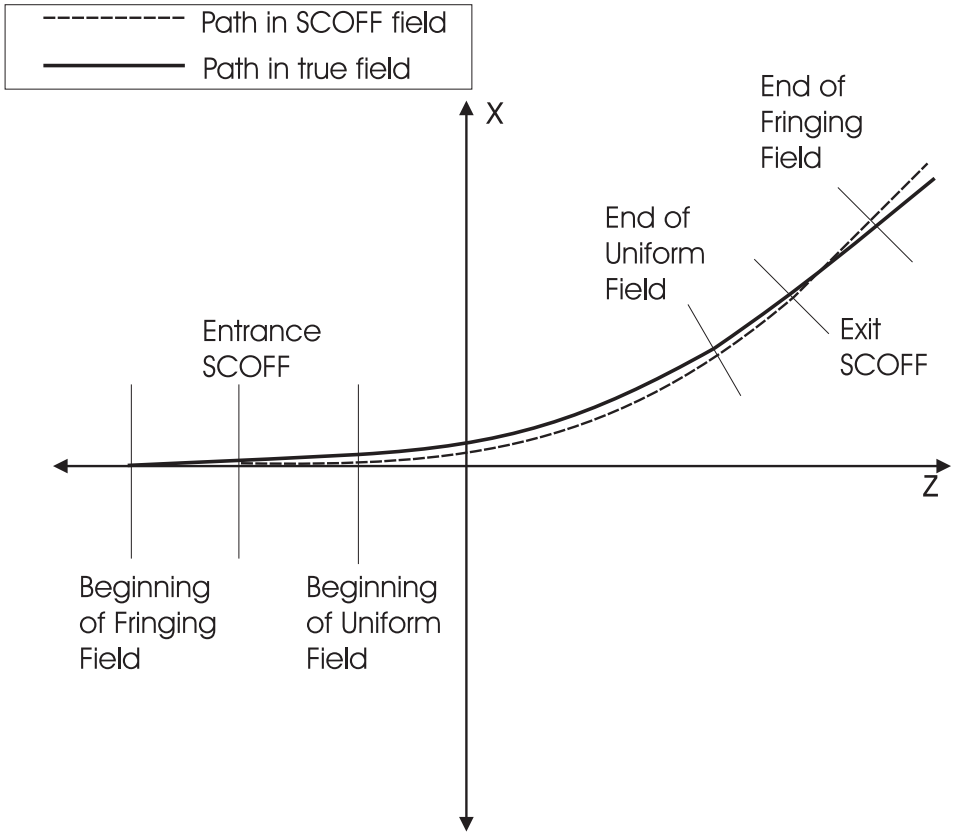

Figure 14: The path of an electron through the measured field compared with the circular path it would take in a uniform SCOFF field. The radius of curvature changes constantly in the fringing field regions, leading to offsets at the effective field boundaries.

3.4 The Spectrometer

The position and direction of the electron beam at the exit portal of the 90-B beam line of the linac are determined by a rotating wire profile monitor, which is designed to rotate so that it crosses the beam in both the horizontal and vertical directions. For initial alignment, a laser was set up at a distance of 5 m from the exit window. A shutter was placed between the laser and the profile monitor, and was triggered to open whenever the monitor passed through the horizontal or vertical centre, exposing the monitor wire to the laser light. The laser was adjusted until the centre of the beam illuminated the profile monitor as it made its sweeps in both the horizontal and vertical planes. Once the laser had been aligned with the profile monitor, two sets of cross-hairs were placed between it and the linac and centred on the laser beam, optically defining the 0^o or "straight-through" axis for the spectrometer. The aluminum alignment plate was then placed on the bottom pole face, and the optical alignment tool was set in the 0^o groove. The laser was replaced with a telescope which was aligned with the two cross-hairs. The position of the magnet was adjusted until both sights in the alignment tool were aligned with the crosshairs.

After the alignment of the magnet was completed, the alignment tool was moved to the 45^o groove, and the telescope was placed opposite, about 4 m from the magnet. Again, two sets of crosshairs were placed between the magnet and the telescope, and aligned with the sights of the alignment tool. This optically defined the 45^o axis.

For the magnet to be used as a spectrometer, the path of the beam through the magnet had to be well defined. To this end, analyzing slits were placed at both the entrance and exit sides of the magnet. Each slit comprised two 2 cm thick copper rods. The position of each rod was controlled by an electric motor connected to a remote controller. By changing the rod positions, both the gap size and its offset from the central axis could be changed and read out remotely. Gap size was calibrated by closing the slits on stainless steel slabs of known thickness.

Before the vacuum box was put in place and the magnet reassembled, the entrance slit had to be aligned with the 0^o axis. The slit was closed to provide a small gap, and the offset was changed until the gap was aligned with both crosshairs, as viewed through the telescope.

With the entrance slit in place, the vacuum box was adapted to the linac, and the magnet reassembled. The exit slit was then fixed to the vacuum box, and aligned with the 45° axis in the same manner as the entrance slit was aligned with the 0° axis. The vacuum box was then sealed, and the beam line pumped down to create a vacuum. Mechanical measurements of the slit jaw positions outside the beam pipe were made and used to verify slit positions after pump-down.

The magnetic field was controlled by a second Rawson probe (Rawson Lush model 920) placed as closely as possible to the centre of the magnet. This probe was connected to an F8 microcontroller. If the reading from the controlling Rawson probe decreased, the magnet current was increased to compensate, and *vice-versa*. In this way, the magnetic field could be controlled to better than 0.01%.

While the Rawson probe provided excellent precision in controlling the magnetic field, the absolute calibration of magnetic field was based on an NMR probe (Sentec Type 1000) which was known to be accurate to better than one part per million (ppm). From NMR measurements, a calibration factor of $(1.7192 \pm 0.0001) \times 10^{-2}$ gauss per Rawson unit was determined. For the larger probe used in the fringing field measurements, the calibration factor was found to be 1.999 gauss per Rawson unit.

The next step was to confirm proper operation of the spectrometer. To align the electron beam along the 0° axis, a scintillating phosphor was placed over the 0° exit window. A hole in the centre of the phosphor was aligned with the crosshairs. With the entrance slit fully open, the beam was centred on the profile monitor and the hole in the scintillating screen. It was then aligned on the 0° axis within ± 0.002 radians. The entrance slit was then closed down to a gap of 2 mm, which was small enough to provide good entrance geometry without scraping the beam.

Current into the spectrometer was measured using a toroidal current monitor (TCM). The exit slit was also closed to a gap width of 2 mm, in order to sharply define the beam path. An aluminum block was used to measure current transmitted through the spectrometer at high beam currents. To acquire an energy spectrum, the magnetic field was set and the currents from the exit monitor and the TCM were integrated for thirty seconds. The ratio of exit current to entrance current was recorded for several magnetic field values. In this

way, a plot of intensity *vs.* magnetic field and hence intensity *vs.* energy could be generated. Equation 5, along with the bending radius of 45.36 cm were used to convert this to an energy spectrum. An example of a measured spectrum is given in figure 15. For low beam currents, such as those required for stopping power measurements, a plastic scintillator was used to measure exit current; the entrance current was too weak to monitor accurately. Changes in accelerator beam current might have been expected to skew the energy peak. However, the centroid of the measured spectrum was found to be constant to within 0.1% over the course of several runs. Zero degree alignment was confirmed by placing a small lead collimator at the "straight-through" position, and a second plastic scintillator was used to measure the beam current transmitted through this collimator. The magnetic field was varied by a few gauss in each polarity to sweep the beam over the collimator slit. The field which provided maximum transmission was used to determine the horizontal offset of the beam at the collimator. From there, any corrections to the measured energy due to steering could be determined (see equation 17). The correction was always less than 0.2%. A schematic of the spectrometer is shown in figure 16. Examples of spectra measured at low currents at 10 and 20 MeV are given in figure 17.

3.4.1 Summary of Ray Tracing Results

ESPLINE was compared with RAYTRACE for the specific test case of a magnet with circular pole faces. The fringing fields were assumed to be sharply cut off. Successive calculations were run to determine the magnetic field necessary to deflect a 20 MeV electron beam through 45°. The two programs gave results which agreed exactly with each other and also with the expected value from equation 3. Further tests were conducted using the measured fringing field data and assuming a circular magnet. Again, the two programs agreed exactly in predicting the field strength required to deflect a 20 MeV electron through 45°.

RAYTRACE was chosen for most calculations because of its more complete treatment of magnetic field calculations and more flexible geometric modeling. In addition to providing a conversion from magnetic field to electron energy, RAYTRACE was also used to estimate the energy resolution of the spectrometer and uncertainties in energy calibration arising from uncertainties in beam geometry.

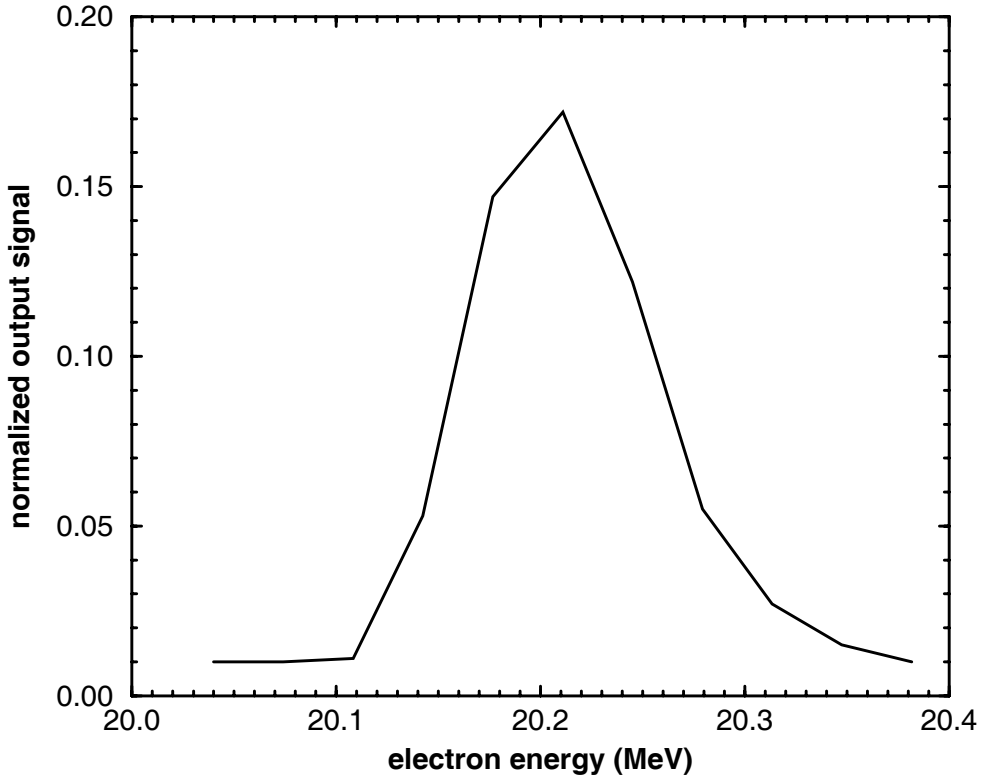

Figure 15: Sample of typical electron energy spectrum at 20 MeV, measured at high beam current.

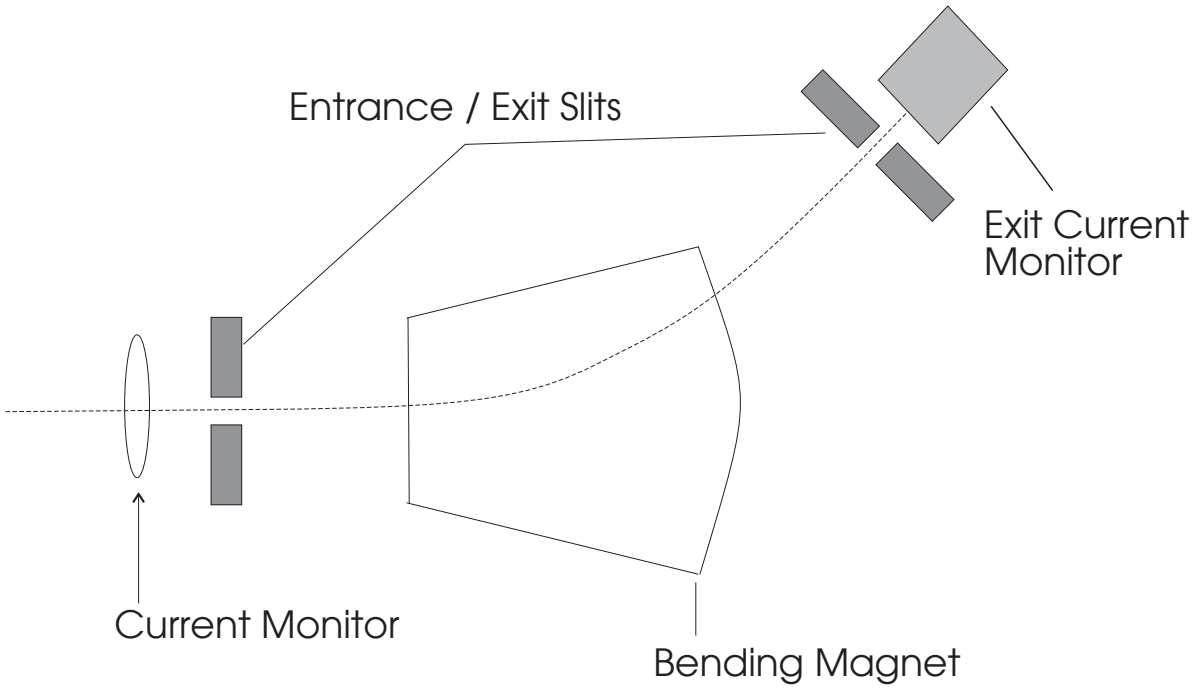

Figure 16: Schematic of magnetic spectrometer.

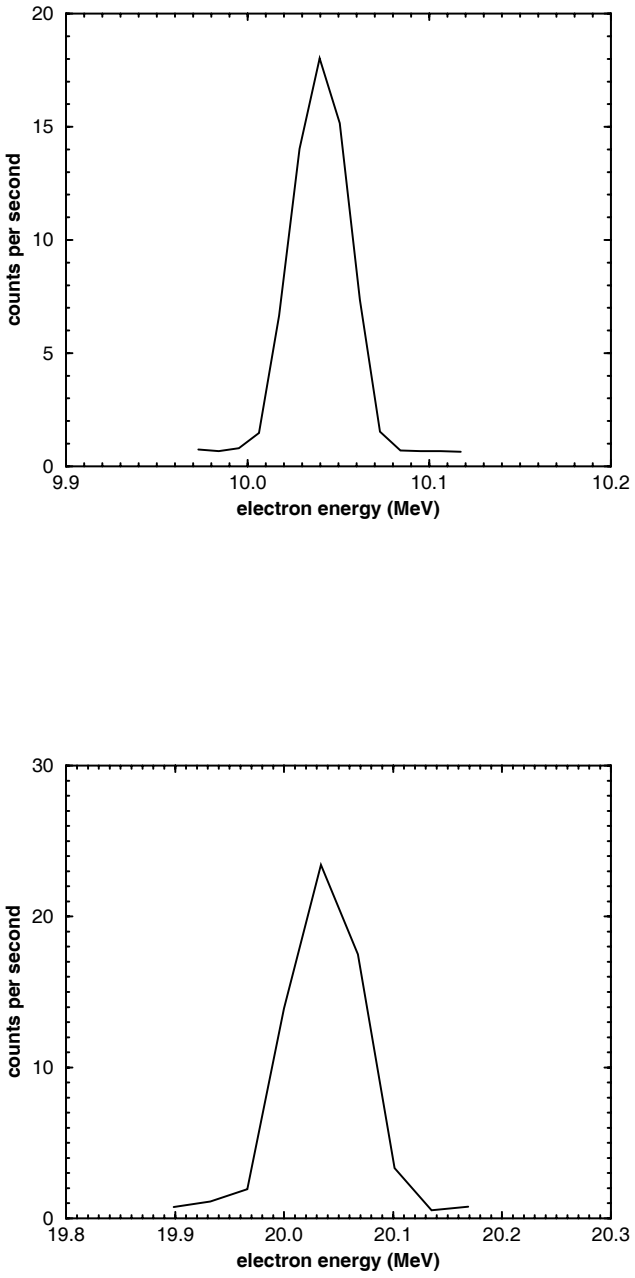

Figure 17: Electron spectra at 10 (top) and 20 MeV (bottom) measured at low beam current (tens of electrons per second). The M1 and S1 slits were each set at 0.2 cm.

Several parameters could affect the final energy measured by the spectrometer, including slit size, beam spot size, entrance offsets in the horizontal plane, angular deflections and divergence, and the intrinsic energy distribution of the beam. The effect of slit size could be determined directly from RAYTRACE simulations. The change in measured energy with respect to offsets in the horizontal plane was found to be

$$\frac{1}{E}\frac{\partial E}{\partial x} \approx 0.01 \text{ cm}^{-1}, \tag{16}$$

at both the entrance and exit slits. From this we conclude that each 2 mm slit corresponds to $\pm 0.1\%$ in energy. The change in energy with respect to entrance angle was

$$\frac{1}{E}\frac{\partial E}{\partial \theta} \approx 0.001 \text{ mrad}^{-1}. \tag{17}$$

The overall uncertainty due to geometric effects was estimated as follows. First, the intrinsic resolution of the spectrometer is due to the finite width of the exit slit. A monoenergetic beam incident on the straight-through axis would appear to be 0.2% wide due to the 2 mm exit slit gap. This is an absolute limit on the precision of the instrument. Extra uncertainty arises due to uncertainties in beam entrance geometry and beam width at the exit slit. The entrance geometry is constrained to 2 mm by the entrance slit, which corresponds to $\pm 0.1\%$. However, this represents a worst case; the standard (1σ) uncertainty is assumed to be 0.05%. In order to measure beam size and estimate the divergence, Gaf-chromic film was mounted to the 0^{o} exit window of the spectrometer, and irradiated at an electron current of 80 nA for 10 seconds. The measured spot was less than 3 mm in diameter. Assuming the same beam size at the exit slit (for a given energy), makes the distribution 0.3% wide (full width at tenth maximum). Again, this is a worst case, and the standard uncertainty is estimated at 0.1%. Considering that the spot was measured nearly 2 m upstream of the entrance slits, the maximum divergence of the beam must be less than 1 milliradians or 0.1%. The uncertainty due to beam divergence is taken as 0.05% (1σ). These geometric effects were added in quadrature with one half of the magnet's resolution (i.e. 0.1%) to give a geometric uncertainty of 0.16%. A more conservative estimate places this uncertainty at 0.2%.

3.4.2 Residual Magnetic Fields

The final energy measured for the electron beam depends on its entrance angle relative to the magnetic spectrometer. The beam was aligned with the scintillating screen by adjusting the steering in the 90-B beam line with the magnet set to zero field. At low energies, this could lead to alignment problems, as the beam is deflected by the earth's magnetic field and residual fields outside the magnet due to hysteresis and magnetization of materials in the beam line. In such a case, the beam would be steered into the magnet at some non-zero angle to compensate for the deflection. Figure 18 show measured residual fields after applied magnetic fields of 400 and 1500 gauss for the entrance and 0^o exit portals, respectively. The average field over the entire range is approximately 1.5 gauss on each side and is not greatly reduced by a simple degaussing of the magnet. The maxima correspond to the positions of flanges where the beam pipes are joined to the vacuum box, suggesting that the bolts which fasten the flanges have been magnetized.

As discussed above, these residual fields result in an alignment error for the beam, whose impact on the energy calibration can be determined as follows. Consider the case where the electron beam enters the magnet precisely on the "straight-through" axis. Due to deflections caused by the residual magnetization, the beam will appear offset a distance $\Delta x_{\rm resid}$. The beam entrance angle must then be adjusted by $\theta_{\rm corr} = \Delta x_{\rm resid}/D_{\rm mag}$ where $D_{\rm mag}$ is the distance over which the particle is under the influence of the residual field (figure 19). $\Delta x_{\rm resid}$ can be estimated as follows. For small angles

$$R_{\rm resid} = (R_{\rm resid} + \Delta x_{\rm resid}) \cos\theta_{\rm resid},$$

where $R_{\rm resid}$ is the bending radius of the residual field. One can write

$$R_{\rm resid} \approx (R_{\rm resid} + \Delta x_{\rm resid})(1 - \frac{\theta^2_{\rm resid}}{2}),$$

from which

$$\Delta x_{\rm resid} \approx R_{\rm resid}\frac{\theta^2_{\rm resid}}{2}. \tag{18}$$

The effect of the residual fields was estimated by treating the residual fields as a constant 1.5 gauss over 40 cm, followed by a 30 cm zero field region (i.e. inside the pole faces), then another 1.5 gauss, 40 cm field. At 5 MeV, in the entrance region, the change in position is

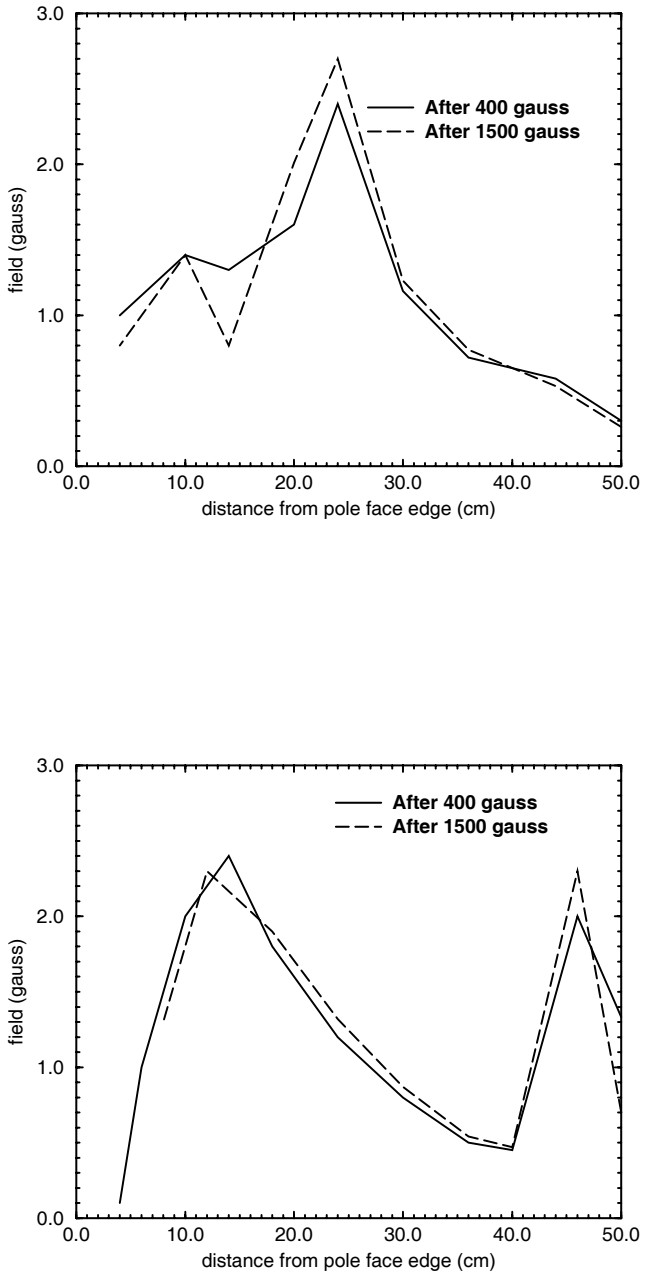

Figure 18: Residual fields on the entrance (top figure) and exit (bottom figure) side of the magnetic spectrometer, as measured after applied fields of 400 and 1500 gauss. The peaks correspond to the location of the beam pipe flanges.

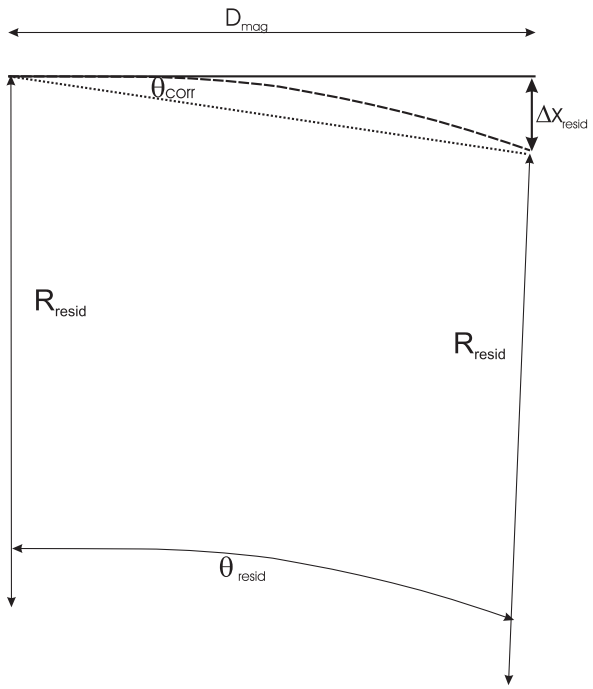

Figure 19: Residual fields lead to an offset ($\Delta x_{\rm resid}$) with respect to the "straight through" path through the spectrometer (solid line). This results in a correction in steering $\theta_{\rm corr}$. $\rm D_{mag}$ is the distance from the profile monitor to the exit phosphor.

0.06 cm and the change in angle is 3 milliradians. Inside the pole faces, this change in angle leads to a further 0.1 cm offset, followed by another 0.06 cm change in the exit field. The net offset is just over 2 mm, for a steering correction of 2 milliradians, or 0.2% (equation 17). The effect is lessened at higher energies.

3.4.3 Earth's Magnetic Field

The value for the earth's magnetic field is approximately 0.55 gauss, opposite to the direction of the applied field of the spectrometer. This causes a decrease in required magnetic field due to steering effects as discussed in the previous section (figure 19). This effect is somewhat reduced by a similar shift in beam position at the exit slit. The net impact of the earth's field on energy calibrations can be estimated as the sum of these entrance (steering) and exit (offset) effects. The steering effect was estimated assuming the earth's field acted over a distance of 2 m. The exit offset was estimated assuming the earth's field acted over a distance of 1 m (from the pole face to the exit slit). Table 3 summarizes the geomagnetic field corrections for each energy.

4 Results and Discussion

4.1 Energy Calibration of the Linac

This project was initiated with the expectation of performing a one-time calibration of the 90-B beam line of the NRC linear accelerator. Before proceeding, a brief description of this portion of the accelerator is in order. The 90-B beam line normally is used for dosimetry of high energy electrons and x-rays. It consists of two dipole magnets, each of which deflects the electron beam through 45°(figure 20). Between the dipole magnets is a slit system which restricts the energy range transmitted through the magnet system, along with a quadrupole magnet which counteracts divergence of the beam. The two dipoles are connected in series, and current to the dipoles is monitored externally with a digital voltmeter (DVM). Changing the magnetic fields of the dipoles also changes the electron energy which can be transmitted through the beam line. It was hoped that the current delivered to the dipoles could be

Energy (MeV)	R_{earth} (cm)	Entrance Effect (Steering)	Exit Effect (Offset)	Net correction
5	33000	+0.15%	-0.3%	-0.15%
7	45000	+0.1%	-0.2%	-0.1%
10	64000	+0.08%	-0.15%	-0.08%

Table 3: Corrections required for the effect of the earth's magnetic field. At energies greater than 10 MeV the corrections are negligible.

related to electron energy with sufficient accuracy for the stopping power work (i.e., better than 0.5%). Early measurements of electron energy showed rather large residuals when compared with the measured magnetic fields inside the 90-B bending magnets. Furthermore, the reproducibility of beam energy for a given 90-B magnet setting was poor, and changes in energy of up to 1% were observed. To understand these effects, it is necessary to look more closely at the geometry of the bending optics of the 90-B beam line.

The linear accelerator consists of four waveguide sections in which the electrons are accelerated. Electron energy is controlled by adjusting the RF power to each section, as well as the relative phase between each section. The direction of the electron beam is controlled by steering magnets located upstream of the dipole assembly. When the dipole current is set, both the steering and waveguide phase are adjusted to allow transmission through the slit system S1 and onto the profile monitor at the end of the beam line. However, the entrance to the bending magnet system is not well defined either in terms of angle or position. As a result, the beam could have lateral shifts of up to 2 cm from the centre of the beam line, and angular displacements of up to 9 mrad. RAYTRACE was used to simulate the path of the electron beam through the 90-B beam line. First-order approximations were used with respect to the dipole magnets. Measurements of the dimensions of the quadrupole were used to describe the quadrupole effect. The magnetic field inside the quadrupole was estimated by varying the quadrupole field in the simulations until the beam was focused at the M2 magnet. The quadrupole had no impact on the mean transmitted energy.

Simulations of the bending system indicate that offsets such as those previously discussed could translate into energy differences of $\pm 0.7\%$. It is likely that the observed 1% energy shift was caused by a change in geometry being compensated by a change in energy (phase adjustments). This problem has been partially resolved by introducing an entrance slit system upstream of the M1 magnet, so that lateral drifts are minimized. The M1 slit consists of movable thick aluminum jaws, and provides a range of entrance widths from 0.2 cm to several cm in both the horizontal and vertical directions. The effect of the M1 slit on transmitted the energy spectrum is modest (figure 21). With the slit closed down to 0.2 cm, variations in observed beam energy are on the order of $\pm 0.2\%$. This is at the cost of a large reduction in transmitted beam current, which may not be desirable for applications

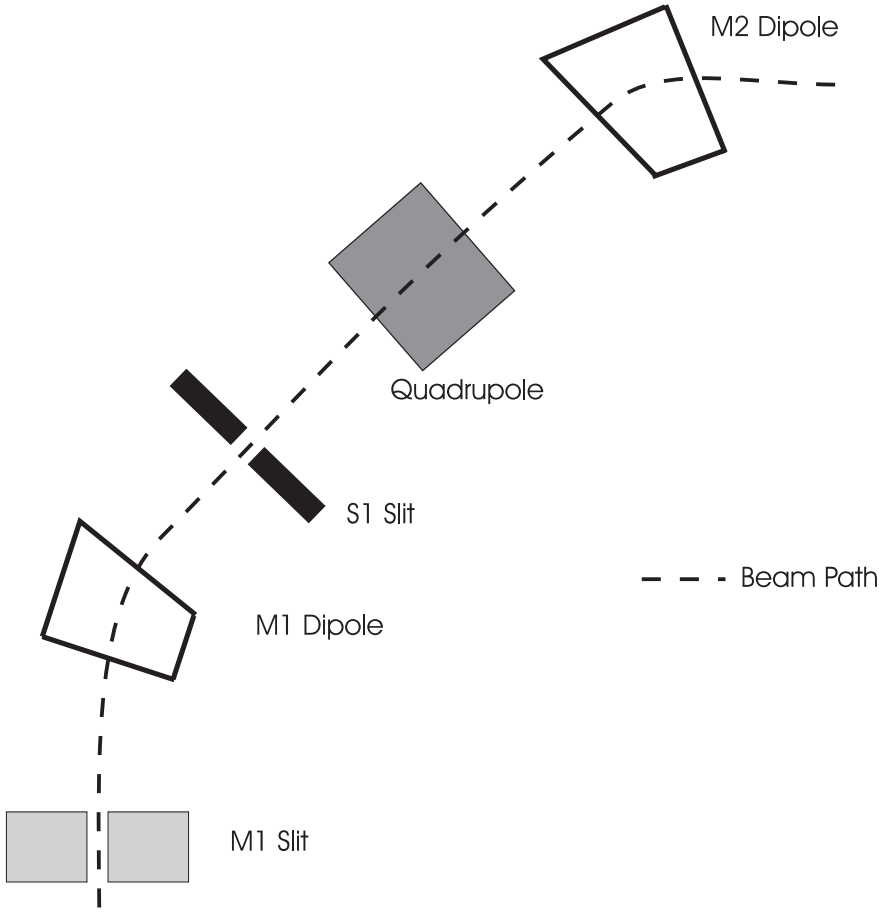

Figure 20: Schematic of 90-B beam line. The dipoles each deflect the beam through 45°, while the quadrupole corrects for dispersion of the beam introduced by the dipole M1. Energy spread is controlled by the slit, S1.

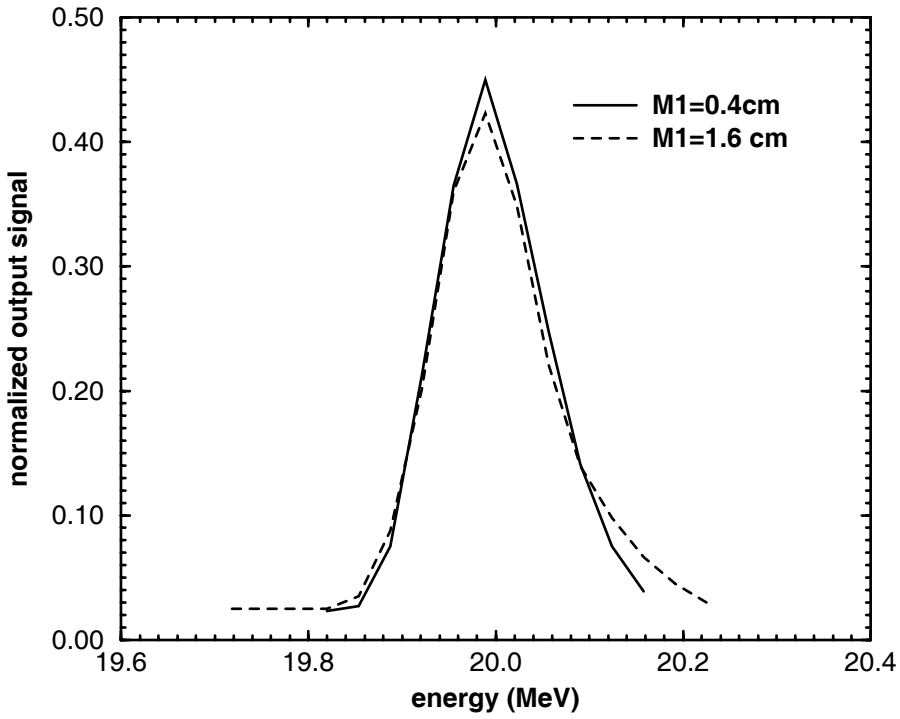

Figure 21: Variation in transmitted spectrum with width of M1 slit. The S1 slit has been set to 0.4 cm. Closing the M1 slit from 1.6 cm to 0.4 cm has no appreciable impact on the measured spectrum.

where high dose rates are required.

With the M1 slit, transmitted energy T was found to vary roughly linearly with the reading of the DVM, V_{M}. The equation

$$T \;=\; 22.77 V_{\mathrm{M}} \;-\; 0.00088, \tag{19}$$

will predict energy to within 0.4% from 5 to 30 MeV (figure 22). The corresponding relationship given in (1) was

$$T_{\mathrm{old}} \;=\; 22.36 V_{\mathrm{M}} + 0.0850. \tag{20}$$

The difference between the old and new calibrations can be written as

$$\frac{T - T_{\mathrm{old}}}{T} \;=\; 0.0180 - \frac{0.0859}{T}. \tag{21}$$

For a given setting of V_{M}, the new, more accurate calibration gives electron energies that are 0.1%, 0.9%, and 1.4% higher than the old calibration at 5, 10, and 20 MeV, respectively. Although this result suggests that previous assignments of electron energies should be increased, it is important to note that the new calibration was done with the M1 slits in place. Without the M1 slits, variations in energy of up to 1% were noted, and this uncertainty would have to be considered in any retrospective evaluation of energy. The largest error seems to reside in the 5 MeV point. This might be expected, as the non-linearity of equation 5 is greatest at low energies. A more robust calibration would relate the actual field inside the M1 magnet to transmitted energy. At each energy, a measurement of the field inside the M1 magnet was made using a Rawson rotating coil magnetometer. The M1 field was found to vary linearly with V_{M}:

$$B_{\mathrm{M}} \;=\; 2.270 V_{\mathrm{M}} + 0.0467, \tag{22}$$

where B_M is in kG. The 90-B optics were approximated as a single dipole, and the effective bending radius was determined at each energy using equation 4 (figure 23). The effective radius at 5 MeV is 0.5% higher than the average of the other points. This may reflect effects of the earth's magnetic field or hysteresis effects at the 90-B dipoles which have not been taken into account. A global fit of B_M and T from 7 to 30 MeV according to equation 5 gives an effective bending radius of 33.51 cm. Therefore, the equation

$$T = \sqrt{101 {B_M}^2 + 0.2611} - 0.511 \tag{23}$$

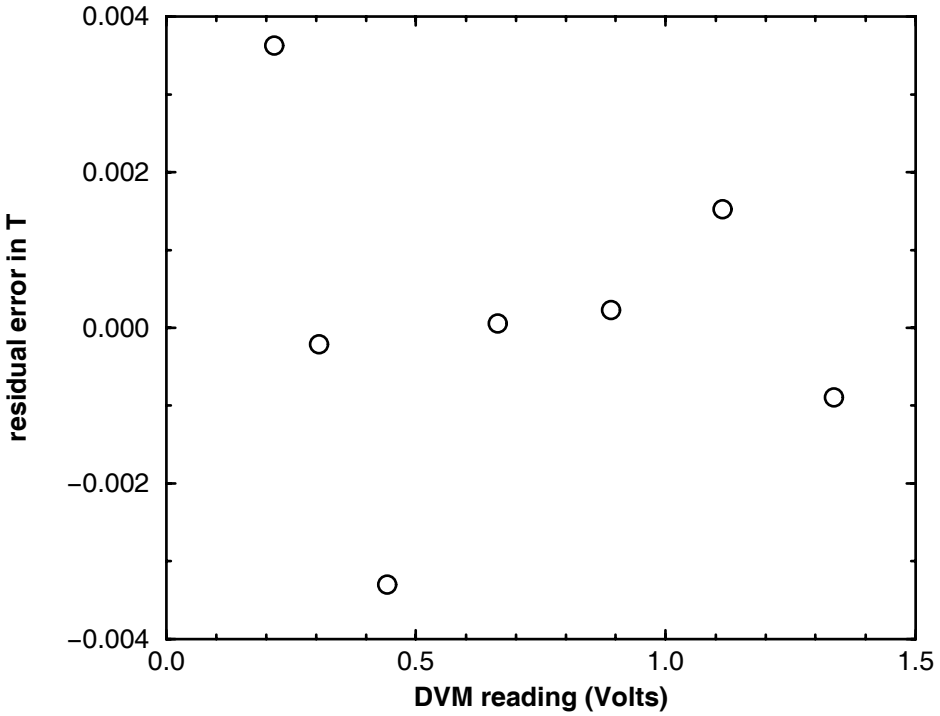

Figure 22: Residuals from a linear fit of electron energy to M1 magnet current as measured using the DVM.

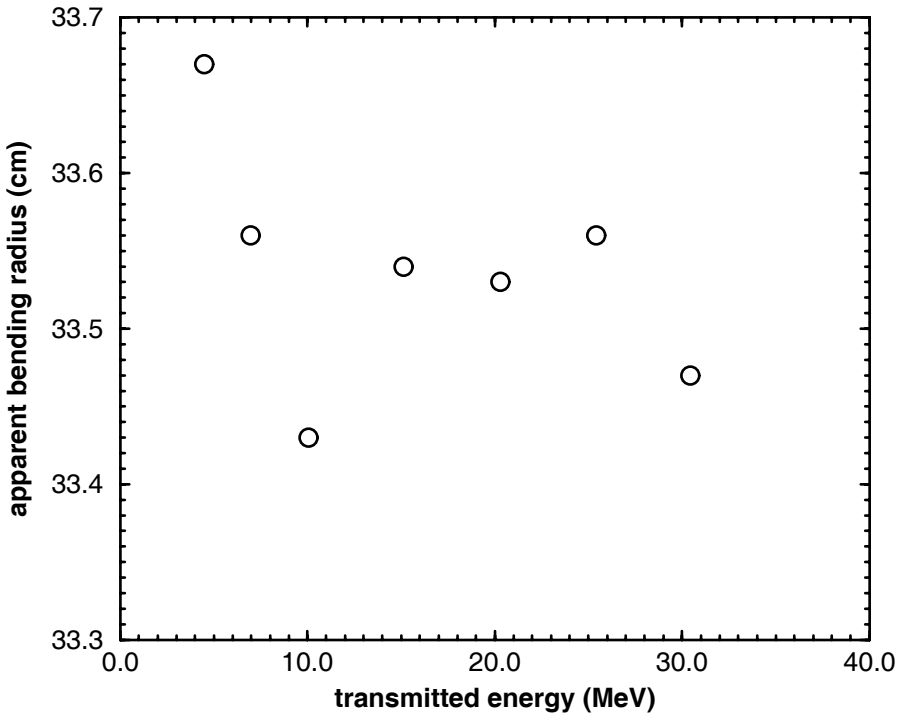

Figure 23: By treating the 90-B dipole assembly as a single dipole, an effective bending radius was calculated at each energy. The 5 MeV point does not agree well with those calculated at other energies.

will predict electron energy from 7 to 30 MeV within 0.25%. Combining this with equation 22 gives the somewhat complicated

$$T = \sqrt{520.4{V_{\mathrm{M}}}^2 + 21.41V_{\mathrm{M}} + 0.4811} - 0.511, \tag{24}$$

which offers improved accuracy over equation 19. However, the uncertainty in the latter is still a factor of at least 2 less than an earlier attempt at this calibration, which relied on range measurements in water (1).

4.2 Beam Characteristics

The magnetic spectrometer presented an opportunity to study in detail the properties of the accelerator beam. Energy spreads in the beam are controlled by the slit system S1 depicted in figure 20. The approximate spread in the beam was known, but no means of testing was previously available. Electron spectra were acquired at 10 MeV for various slit openings, with the M1 entrance slit set to 0.2 cm. The transmitted current was observed to decrease as the slit was closed, and the energy spread decreased from about 3% FWHM for a 1.6 cm slit opening to about 0.4% FWHM for a slit opening of 0.2 cm (figure 24). Some of this residual width is attributed to the intrinsic resolution of the spectrometer (0.2%) and the effect of the finite width of the beam (estimated at 0.2%). By combining these effects in quadrature, the energy spread of the incident beam is estimated to be 0.3% at FWHM.

4.3 Error Analysis

The measured fringing fields are expected to be accurate in terms of position to within 0.5 mm on each side. This corresponds to a ±0.2% uncertainty in energy. The intrinsic resolution and uncertainties due to beam geometry have been combined to estimate the "geometric" uncertainty in the measured energy at 0.2%. Uncertainties in bending angle (which impacts on the calculated design radius and, ultimately, on energy), magnetic field, and the effect of vacuum box contribute less to the overall energy uncertainty, which is about 0.3%. Table 4 summarizes the uncertainties associated with the energy measurement.

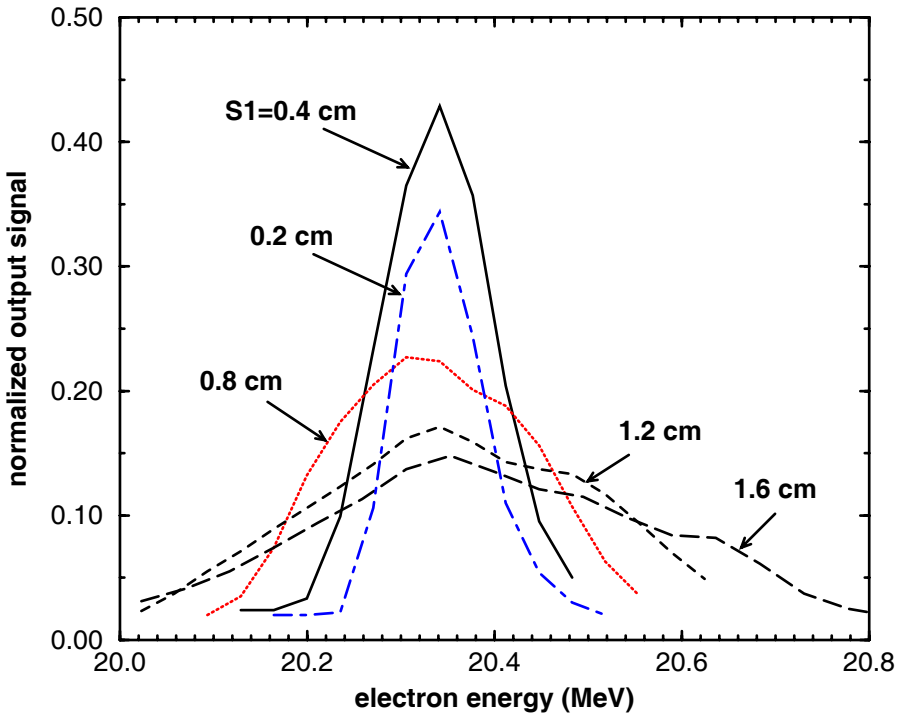

Figure 24: Variation in transmitted spectrum with width of S1 slit. The M1 slit has been set to 0.4 cm. Closing the S1 slit from 1.6 cm to 0.2 cm reduces the FWHM of the transmitted spectrum from 2.5% to 0.4%.

Intrinsic resolution and beam geometry	0.2%
Magnetic field	0.01%
Entrance/exit fringing fields	0.2% ($\pm$0.5 mm each side)
Stainless steel vacuum box	0.05%
Quadratic sum	$\approx$ 0.3%

Table 4: Breakdown of uncertainties related to energy calibration. All uncertainties are estimated as 1σ.

5 Conclusion

A magnetic spectrometer has been constructed and adapted to the 90-B beam line of the NRC electron linear accelerator. The spectrometer consists of a dipole magnet which deflects the electron beam through 45°. The intrinsic resolution of the spectrometer is 0.2%, and the uncertainty in measured energy (which includes uncertainties due entrance geometry, beam size and fringing fields) is estimated to be ±0.3%. This level of uncertainty represents a factor of 3 improvement over the previous electron energy calibration, and is sufficiently small to allow precise measurements of electron stopping powers.

The spectrometer has revealed reproducibility problems in transmitted energy at the 90-B beam line, which have been attributed to variations in beam position at the entrance to the 90-B optics. A beam-defining slit has been added before the 90-B magnets, which improves reproducibility in energy to better than 0.2%, albeit at the cost of transmitted current.

The full width at half maximum (FWHM) of the electron beam at the exit window of the accelerator depends on the amount of geometrical restriction imposed by the S1 slit of the 90-B bending magnets. The full width at half maximum of the energy spread of the electron beam varies from nearly 3% with a 1.6 cm slit opening to 0.3% with the slit closed to 0.2 cm.

Electron energy at the 90-B beam line has been calibrated in terms of current supplied to the 45° dipoles. The energy predicted from the new calibration is up to 1.5% higher than that estimated using an earlier calibration. However, without the new beam defining slit, energy changes of 1% are possible. This should be considered in any re-evaluation of work based on the old calibration.

Acknowledgements

The authors are grateful to Matt Kosaki, Leo Heistek and David Marchington for their able technical assistance throughout this project. Thanks are also due to Dr. Len Van der Zwan for sharing his experience with the magnet. Dr. Joe Deasy provided helpful discussions on ray tracing algorithms.

References

[1] C. K. Ross and K. R. Shortt, Energy calibration of the 90-B beam line of the IRS linac, NRC Report PIRS-0021, National Research Council of Canada, Ottawa, Canada, 1985.

[2] B. B. Sorcini and A. Brahme, An accurate energy-range relationship for high-energy electron beams in arbitrary materials, Phys. Med. Biol. **39**, 795 – 811 (1994).

[3] B. B. Sorcini, P. Andreo, A. F. Bielajew, S. Hyödynmaa, and A. Brahme, An improved energy-range relationship for high-energy electron beams based on multiple accurate experimental and Monte Carlo data sets, Phys. Med. Biol. **40**, 1135 – 1159 (1995).

[4] N. Blais and E. Podgorsak, The mass angular scattering power method for determining the kinetic energies of clinical electron beams, Phys. Med. Biol. **37**, 1931–1942 (1992).

[5] C. E. de Almeida and P. R. Almond, Energy calibration of high energy electrons using a Cerenkov detector and a comparison with different methods, Phys. Med. Biol. **19**, 476–483 (1974).

[6] L. B. Levy, R. G. Waggener, and A. E. Wright, Measurement of primary bremsstrahlung spectrum from an 8-MeV linear accelerator, Med. Phys. **3**, 173–175 (1976).

[7] J. Brownridge, S. Samnick, P. Stiles, P. Tipton, J. Veselk, and N. Yeh, Determination of the photon spectrum of a clinical accelerator, Med. Phys. **11**, 794–796 (1984).

[8] J. J. Battista, *A Magnetic Spectrometer for Betatron Electrons*, M. Sc. Thesis, The University of Western Ontario, London, Canada (1973).

[9] B. B. Sorcini and S. Rosander, Energy distributions from a racetrack microtron measured with a magnetic spectrometer, Med. Phys. **20**, 695–702 (1993).

[10] J. J. Livingood, *The Optics of Dipole Magnets*, Academic Press, New York, 1969.

[11] A. Septier, *Focusing of Charged Particles, Volume I*, Academic Press, 1967.

[12] P. Lorrain, D. Corson, and F. Lorrain, *Electromagnetic fields and waves*, W. H. Freeman and Company, New York, 1987.

[13] S. Kowalski and H. A. Enge, RAYTRACE, MIT report, Laboratory for Nuclear Science, Massachussets Institute of Technology, Cambridge, Massachussets, 1987.